Lab on a Chip

PAPER

View Article Online
View Journal

Cite this: DOI: 10.1039/c6lc00703a

Large scale flow visualization and anemometry applied to lab-on-a-chip models of porous media†

Johan Paiola,[ab] Harold Auradou*[b] and Hugues Bodiguel[ac]

The following is a report on an experimental technique that allows one to quantify and map the velocity field with very high resolution and simple equipment in large 2D devices. Illumination through a grid is proposed to reinforce the contrast in the images and allow one to detect seeded particles that are pixel-sized or even smaller. The velocimetry technique that we have reported is based on the auto-correlation functions of the pixel intensity, which we have shown are directly related to the magnitude of the local average velocity. The characteristic time involved in the decorrelation of the signal is proportional to the tracer size and inversely proportional to the average velocity. We have reported on a detailed discussion about the optimization of relevant involved parameters, the spatial resolution and the accuracy of the method. The technique is then applied to a model porous medium made of a random channel network. We show that it is highly efficient to determine the magnitude of the flow in each of the channels of the network, opening the door to the fundamental study of the flows of complex fluids. The latter is illustrated with a yield stress fluid, in which the flow becomes highly heterogeneous at small flow rates.

Received 31st May 2016,
Accepted 7th June 2016

DOI: 10.1039/c6lc00703a

www.rsc.org/loc

Introduction

One of the challenges of microfluidic technology is the development of tools to characterize flow properties with suitable resolution.[1] For nearly twenty years, the PIV (particle image velocimetry), PTV (particle tracking velocimetry) or LIF (laser induced fluorescence) methods have been successfully adapted to obtain information about the flow at the micro-scale.[2,3] Recent developments have even enabled us to obtain 3D visualizations of the flows allowing an enriched description of the processes.[4,5] However, these techniques are developed in order to have an accurate description of the flow field at the smallest possible scale – the single cell[6] or bacteria scale[7] for instance – but they only cover a limited range of scales. Complex microfluidic devices typically involve tens to hundreds of channels and therefore require a velocimetry or, at least, an anemometry technique having a super-high spatial resolution.

In the past decades, micromodels obtained using transparent microfluidic technology have been widely used[8–21] to model flows in porous media. Thus, this technique allows one to study at the relevant length scales and with a precise control of the geometry flow in porous media and it has permitted significant progress on the understanding and on the description of the flows in those media. However, characterizing flows in micromodels represents a technical challenge, as one needs to perform measurements over length scales ranging from the pore scale up to a scale for which the macroscopic properties of the porous media are reached. For porous media modelled by a disordered channel network, it is assumed that a typical number of one hundred parallel channels is a minimum value to be statistically representative. Under this condition, a single pore only represents from 0.1 to 0.5% of the full scale. As few pixels per pore are necessary to characterize the flow, the resolution rapidly reaches the limit of standard cameras: a few thousands of pixels per dimension. Therefore, flow characterization requires a very good resolution over a wide range of scales, which is in practice difficult to achieve. This issue is likely to be the reason why most of the past studies were either restricted to qualitative observations,[13,21] limited to the measurement of the saturation,[15,12] or considering flow at the scale of a few pores.[11] Only a few studies report quantitative velocity measurements,[10,17] where the authors took advantage of the good contrast existing in biphasic flows. Yet, this technique gives sole access to menisci velocity and does not give information about the flow inside the fluids.

The purpose of this work is to go beyond these limitations and to propose an anemometry technique having an extra-

[a] Univ. Bordeaux, CNRS, Solvay, LOF UMR5258, Pessac, France
[b] Laboratoire FAST, Univ. Paris Sud, CNRS, Université Paris-Saclay, F-91405, Orsay, France. E-mail: auradou@fast.u-psud.fr
[c] Univ. Grenoble Alpes, CNRS, Lab. LRP UMR5520, F-38000 Grenoble, France

† Electronic supplementary information (ESI) available. See DOI: 10.1039/c6lc00703a

high resolution. Although it has been developed to tackle the technical issue of mapping the velocity in a micromodel of porous media, the technique is versatile and could be directly applied to complex microfluidic networks.

When the acquisition device does not capture the full image, one solution is to combine a mosaic of images to reconstruct the complete velocity field. Yet, this procedure is only adapted to steady flows and requires the use of adapted equipment and reconstruction software to combine the images. In this work, by pushing the resolution limit to its minimal value, the pixel size, we were able to avoid reconstruction procedures. To do so, we use the time variation of the light intensity on each pixel rather than space correlation of successive images. The decay of the autocorrelation function of the light intensity is – in the high Péclet limit – related to the local velocity. Pixel resolution can also be reached with micro-PIV.[22,23] This method uses time averaging of space cross-correlations but requires particles not smaller than 3–4 pixels.[24,25] In this work, the use of particle images that are below the pixel size sets the spatial resolution of our technique to one pixel size. As compared to PTV or PIV, only the magnitude of the velocity can be measured. In a network, velocity direction is known *a priori* from channel orientation, so that this disadvantage is not highly relevant in these applications. The main advantage of time autocorrelation is that it requires neither particle detection as in PTV nor uniform and good quality images as in standard PIV. We show in this work that it could be applied on images of poor quality, where particle displacement is hardly visible with the naked eye.

The second issue is to use tracers that do not perturb the flow: particle size should thus not exceed a tenth of the channel width. On the other hand, tracers have to be on the order of the pixel size. This last requirement makes particle detection difficult. One solution is to use fluorescent particles, but their use at the centimeter scale or above is not straightforward and is not accessible by standard fluorescence microscopy equipment. By taking advantage of the schlieren effect,[26,27] our technique avoids the use of fluorescent tracers and only required a standard bright field illumination. It is obtained by simply placing a grid between the device and the light source to detect refractive index differences between the tracers and the fluid. The grid enhances the contrast of the images allowing particle detection even if the particle size is below the pixel size. Despite the contrast enhancement, the images are of poor quality but sufficient for time autocorrelation analyses of the light intensities.

In this paper, we present in detail the principles and the validation of the autocorrelation particle imaging anemometry. The technique is applied to map the velocity field in a complex and wide microfluidic network of channels. We show that the method is simple and fast and importantly leads to highly resolved determination of the mean velocity in all the channels simultaneously. These results and validation are obtained for Newtonian fluids. In order to illustrate the potential use of the technique, we present some results obtained with a yield stress fluid.

Description of methods and materials

System overview

Two microfluidic devices were developed using a classical soft lithography technique.

The first one is a channel of constant depth (h = 340 μm) but of gradually increasing width. The widths (W) are 150, 200, 300, 400 and 500 μm, and the total length of the channel is 10 mm. This device is used to calibrate and validate the autocorrelation technique at the pore scale.

The second one, displayed in Fig. 1, is a square lattice of 110 by 110 channels of rectangular cross sections. The height of the channels is uniform and equal to 200 μm, while their widths are set randomly according to a log-normal distribution with a mean value of 200 μm and a standard deviation of 50 μm (see Fig. 1b). The lattice is orientated at 45°, and N = 100 channels are connected to the inlet. A tree-like geometry made of channels of 2000 μm width is used at the inlet and at the outlet to impose a parallel flow (see Fig. 1a).

The inlet of the device is connected to a syringe pump and the outlet to a waste reservoir. We used either pure glycerol or yield stress fluid obtained by mixing 0.7 g L^{-1} carbopol EDT2050 and water (see ref. 28 for a complete description of the preparation procedure). The flow curve of the carbopol solution has been determined using standard rheometry and is well described by the Herschel–Bulkley law: $\sigma = 15 + 5.10\dot{\gamma}^{0.5}$. The fluids are seeded with transparent beads of PMMA. Two diameters are used: 6 and 20 μm. The concentration is 0.5% (weight fraction) for the 6 μm beads and 0.3% w/w for the 20 μm beads.

A JAI BM 500 GE video camera is positioned above the setup. Its CMOS sensor consists of 2456 by 2058 pixels, and its maximum rate of capture is 7 frames per second in full resolution. It is equipped with a 25 mm objective, with a depth of field of about 1 cm. The spatial resolution of the camera has been varied to test the limitation of the technique, but for the anemometry mapping of the channel network, it is about 25 μm per pixel. This resolution does not permit the visualization and tracking of single particles, but as detailed in the next section, contrast enhancement using a grid allows the detection of intensity fluctuations due to tracer displacement.

Contrast enhancement

To enhance the contrast, we adapted the synthetic schlieren technique[26] developed in the 1990s to measure density fluctuations in two-dimensional stratified flows. In that case, density fluctuations are revealed through small optical refraction index variations enhanced by placing a grid between the light source and the observation field. Our technique uses the refraction index contrast between particles suspended in the fluid and the fluid. This is achieved by placing a grid between a light panel and the device. The grid produces a uniform field of dotted sources of light and the light passing through the beads is refracted, thus reducing the light intensity at that position. The grid is a sieve with a mesh size of

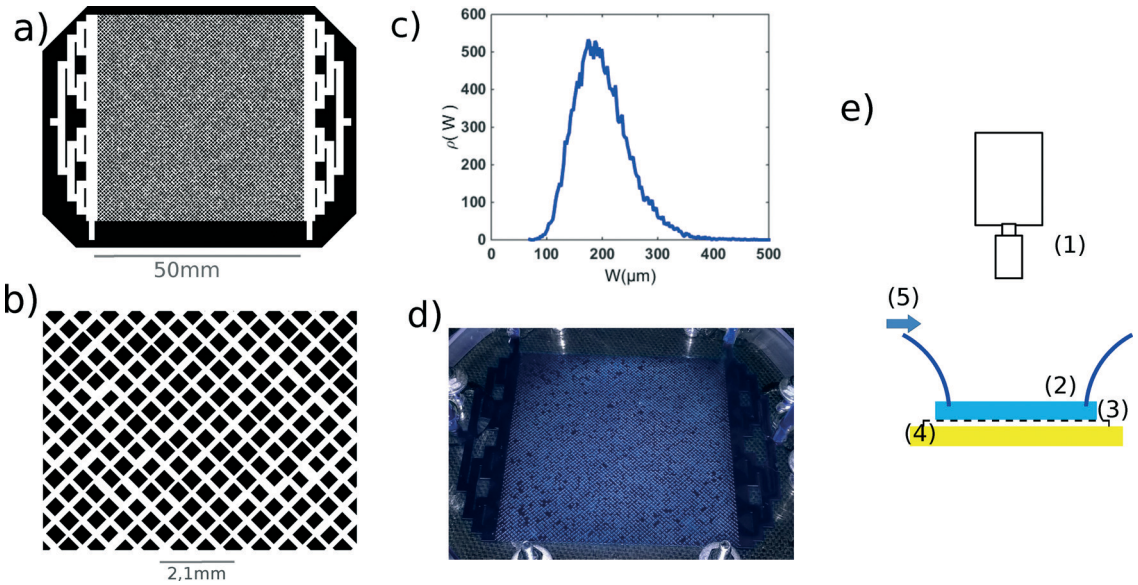

Fig. 1 a) Mask used for lithography. The microfluidic chip consists of a 2D network made of 110 by 110 channels. The average channel width (W), length (l) and depth (h) are 200, 700 and 600 μm, respectively. b) Close-up view of the network. c) Size distribution of the width (W) of the channels in μm. d) Photograph of the assembled microfluidic device filled with a dyed fluid. e) Schematic view of the experimental set-up: 1 – camera with a 25 mm lens, 2 – microfluidic chip, 3 – grid with a square mesh, 4 – light panel, 5 – connections.

20 or 40 μm. Fig. 2 displays two zoomed-in images obtained with and without the grid. The difference between the two images is striking: the beads are visible on the picture taken with the grid, while they are not when the grid is removed. We found that the contrast enhancement is maximal when the grid is placed near the observation plane and when the particles and the mesh of the grid have a similar size. The physical origin of this effect is related to light refraction by the beads. Without the grid, the light panel projects a diffuse light that appears bright from all viewing directions. The grid creates an array of point light sources and deviations of light beams directly modifying the light intensity measured on each pixel.

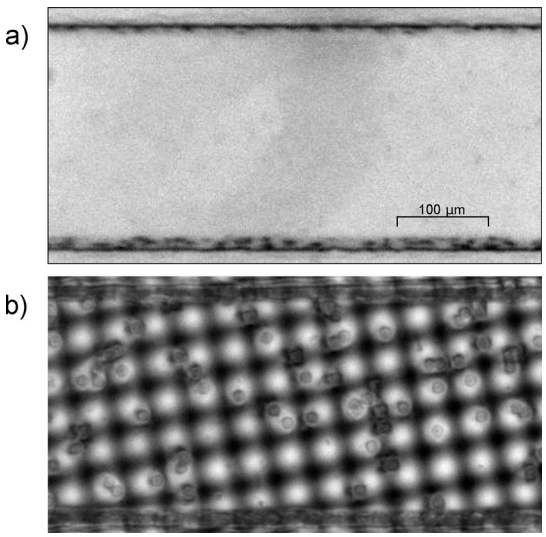

Fig. 2 (a) Close-up view of a single channel. The width of the channel is 250 μm. The channel is filled with glycerol containing PMMA beads of 20 μm diameter. (b) The same view but with a grid added between the light pad and the microfluidic device. The mesh size of the grid is 40 μm. The grey circles are beads. The spatial resolution is 1.15 μm per pixel and the mean flow velocity V = 16 μm s^{-1}.

In the following, we use a lower resolution: the pixel and grid have a similar size. The image quality is thus much lower, and the beads are barely visible to the naked eye. Yet, as illustrated in Fig. 3a, the contrast enhancement is still measurable. The light intensity fluctuations due to particle displacement are difficult to distinguish from background noise in the absence of the grid (dotted line in Fig. 3a) but become visible immediately when the grid is used (solid line in Fig. 3a). We will show below that these fluctuations correspond to the passage of individual beads.

Image treatment

To demonstrate that the fluctuations observed with a grid are due to the passage of the beads on that pixel, we compute the normalized time auto-correlation function of the centered intensity of a single pixel. It is defined by

$$C(x,y,\Delta t)=\frac{\sum_t\left[I(x,y,t)-\langle I(x,y)\rangle_t\right]\left[I(x,y,t+\Delta t)-\langle I(x,y)\rangle_t\right]}{\sum_t\left[I(x,y,t)-\langle I(x,y)\rangle_t\right]^2}, \quad (1)$$

where Δt is the time lag and I is the pixel intensity. The subscript t stands for summation or averaging in time, over the

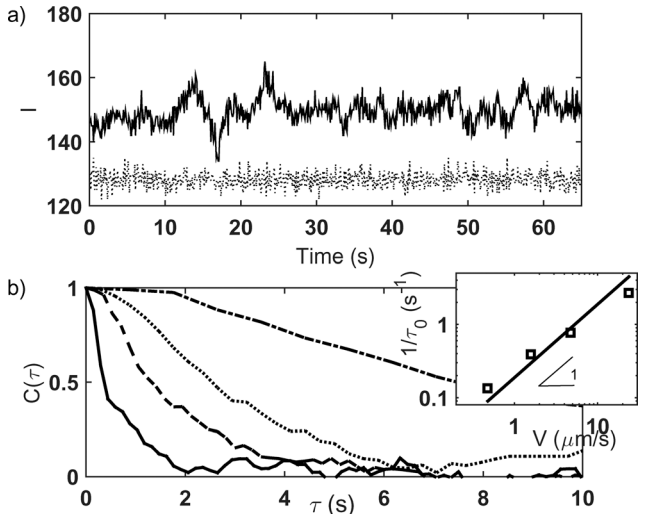

Fig. 3 (a) Variation of the light intensity $I(x, y, t)$ with time. Solid and dotted lines are measurements performed with V = 4.8 μm s^{-1} with and without the grid, respectively. (b) Auto-correlation function C(Δt) in relation to the time lag Δt for V = 23.8 (solid line), 4.8 (dashed line), 1.6 (dotted line) and 0.48 μm s^{-1} (dash-dotted). For these experiments, the bead diameter is 20 μm, and a grid of 40 μm mesh size was used. The spatial resolution is 22 μm per pixel. In the inset, the characteristic time τ_0 is plotted as a function of the mean velocity (see text).

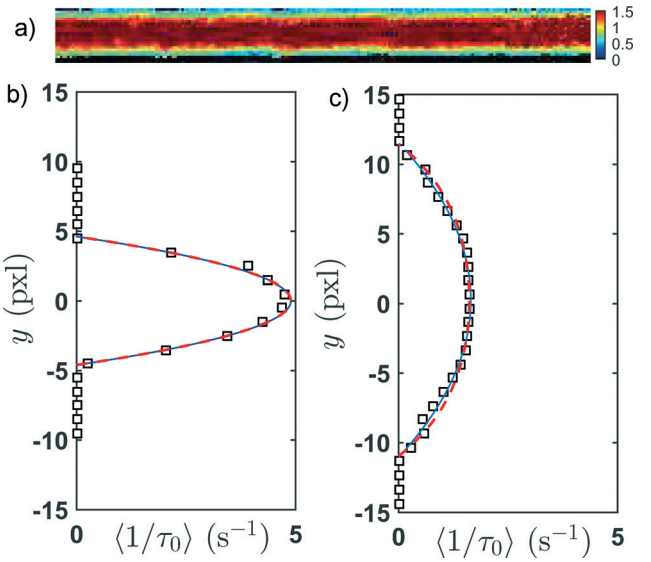

Fig. 4 (a) Color map of $1/\tau_0(x, y)$ measured on each pixel of a channel of 500 μm width and 10 mm length. V = 1.3 μm s^{-1}. (b and c) Profiles of $\langle 1/\tau_0(x, y)\rangle_x$ where x is the coordinate along the flow direction and y is the coordinate normal to the flow. The channel widths are 150 (b) and 500 μm (c). The spatial resolution here is 15 μm per pixel. The diameter of the beads is 6 μm, and the grid mesh size is 20 μm. The solid lines are the best parabolic fit to the data, and the dashed lines correspond to the velocity profile of a channel of rectangular cross-section, averaged over the depth of the channel.

whole image sequence. By construction, these functions decay and eventually vanish at long times. The correlation functions are calculated using Fourier transforms of the intensity, since the computation time significantly decreases. Examples are displayed in Fig. 3b for different flow rates. Clearly, the autocorrelation function decreases faster for high flow rates.

The anemometry technique that is proposed in this article is based on this observation and consists in measuring the characteristic time of the autocorrelation function decay. The latter is estimated as the time τ_0 at which $C(\tau)$ = 0.5, and we use linear interpolation of the autocorrelation function to obtain a better time resolution. The inset in Fig. 3 shows the value of $1/\tau_0$ obtained from the measurements of the correlation functions for different mean velocities (V) in the channel, defined by $V = Q/S$, where Q is the flow rate and S is the channel cross-section. A linear relation between the two quantities is observed, suggesting that it is possible to obtain a local measurement of the fluid velocity from the measurement of the autocorrelation function of the light intensity.

Results

Flow in a single channel

We first applied the technique to experiments performed in straight channels. Fig. 4 shows one of the maps of the inverse of τ_0 that we obtained. At the centre of the channel, τ_0 is small indicating that the beads travelled faster in the central region of the flow. On the sides, the time is large (and $1/\tau_0$ is small); in these regions, the beads travel more slowly. From these maps, we estimate the velocity profiles by averaging $1/\tau_0$ along the flow direction. The profiles are shown in Fig. 4b. They are very well adjusted over the full width of the channels by a parabolic profile as expected for Poiseuille flows in slits. However, the slit approximation is not strictly valid since the channel cross-section is rectangular, with an aspect ratio ranging between W/h = 0.44 and 1.5.‡ If we assume that the measured velocity is averaged over the entire thickness of the channel, the difference between the parabolic profile in a slit and the averaged profile in a rectangular channel is rather small. These are displayed in Fig. 4b, and the difference remains smaller than the measurement uncertainty. Near the surfaces, fluctuations of the inverse of time are larger, emphasizing the difficulty in achieving good measurements close to a surface. The fact that we used beads that are smaller than the pixel size allows us to achieve a spatial resolution of 1 pixel: as shown in Fig. 4b, velocity profile measurement is achieved in a channel which is only 10 pixels wide.

The experiment was repeated for different flow rates, and the average value of $1/\tau_0$ was calculated on all the sub-parts of constant width of the channel. Fig. 5 shows the average value of $1/\tau_0$ in relation to the corresponding average flow velocity. The data fall on a single line passing through the origin. The slope $1/\alpha$ is used to determine the relation between the time τ_0 measured and the current velocity. We find a value of a which is about 10 μm. This length is on the order of both the

‡ In a channel of rectangular cross-section, the flow profile is given by $v(y, z) = \sum_{n=1,3,5\ldots} (1 - \cosh(n\pi y/h)/\cosh(n\pi w/2h)\cos(n\pi z/h)/n^3$ (ref. 29).

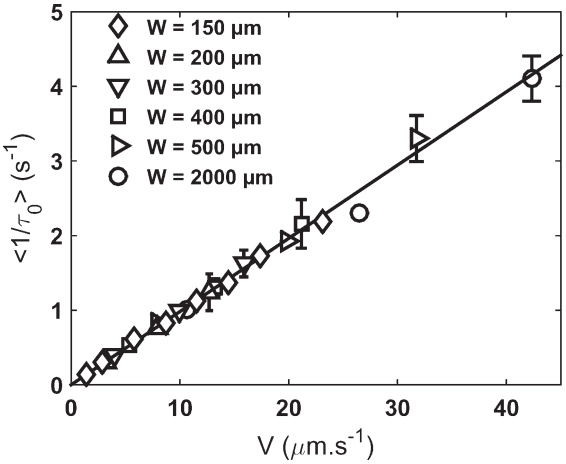

Fig. 5 Each symbol represents the average value of $1/\tau_0$ estimated from each experiment (different flow velocities (V) and channel widths (w)) in relation to the average flow velocity V. The solid line is the linear regression of the measurements. Its slope is $1/\alpha$ with $\alpha = 10.18 \pm 0.25$ μm. The spatial resolution here is 15 μm per pixel. The diameter of the beads is 6 μm, and the grid mesh size is 20 μm. The diamonds represent the measurements performed in the injection channels of the network displayed in Fig. 6. The conditions are the same (bead diameter of 6 μm and mesh size of 20 μm) except for the spatial resolution of 25 μm per pixel instead of 15.

bead size and the pixel size, and this will be discussed later. This result proves the ability of the auto-correlation technique to be used in measuring local flow velocity, after calibration. This study also allows us to estimate the experimental uncertainty in the measurements of the magnitude of the velocity (approx. 5%).

We find that the calibration factor $1/a$ does not depend on the aspect ratio of the channel, as evidenced in Fig. 5. Note that we have significantly varied the channel aspect ratio (W/h) from 0.4 to 3.3. This indicates that the local velocity measured in one pixel is averaged over the channel depth. Due to the large depth of field of the optic, all the beads flowing in the section are thus captured by the camera. The result also shows that the sensitivity of the detection is not influence by the velocity of the particle and that particles are uniformly distributed in the section. Therefore, we conclude that the auto-correlation technique could serve as a local anemometry technique, which is of great interest in complex microfluidic networks since only a few pixels per channel are needed to achieve a precise measurement. It might also be extended for velocimetry application, but one would need to achieve a better optical vertical resolution using for instance confocal microscopy.

Flow in a complex channel network

We next applied the method to the network of channels of random width depicted in the introduction. In this case, the spatial resolution is 25 μm per pixel, and the goal is to measure the velocity over the full size of the chip. The spatial resolution is four times the bead diameter, which means they are not visible, preventing any tracking. Moreover, each channel contains in average only ten pixels, making it difficult to determine a flow profile precise enough for a good estimation of the average flow velocity using the classical techniques.

Despite these obstacles, we were able to obtain a map of the magnitude of the velocities with a good resolution (see Fig. 6), using the calibration displayed in Fig. 5. To quantitatively test our estimation of the flow velocities, we performed experiments at different flow rates and computed the mean value of the velocity in the entire network. The results are shown in Fig. 7a. As for the single channel, the average flow velocity obtained by using our technique varies linearly with the average imposed flow velocity $V = Q/NS$, where N is the number of channels and S is the average cross-section. We note that the mean measured velocity is about 15% higher than V. This over-estimation is not measured when the analysis is performed on the straight channels connecting the

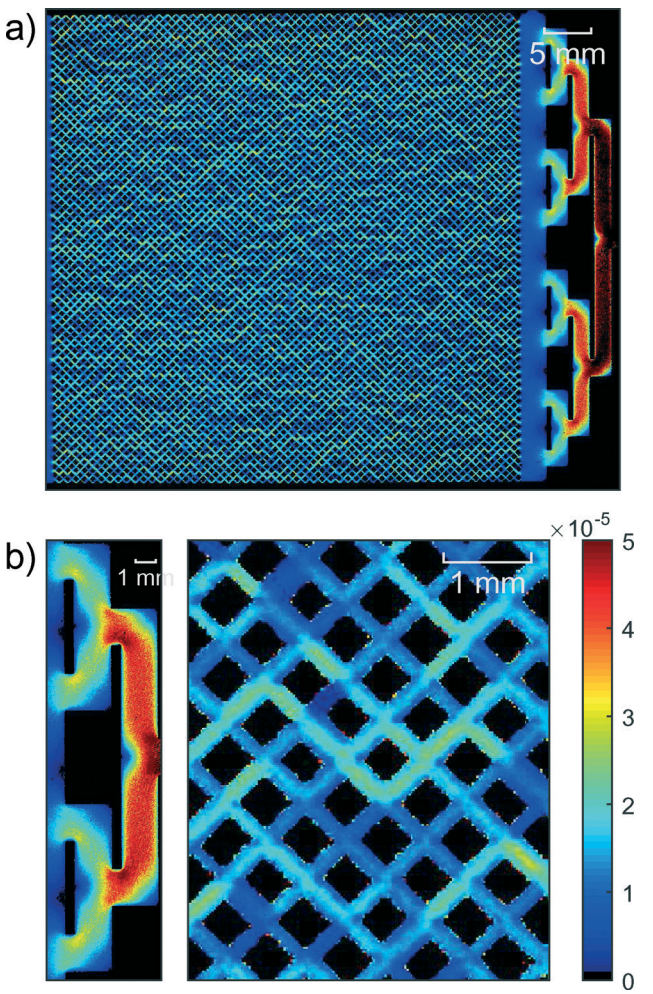

Fig. 6 (a) Color scale map of the flow velocity measured on each pixel. Pure glycerol containing beads of 6 μm diameter is injected at an average flow velocity $V = 6.3$ μm s^{-1} in the micromodel. For this experiment, we used a grid of 20 μm. The spatial resolution is 25 μm per pixel. (b) Close up view of the injection section and that of a part of the network.

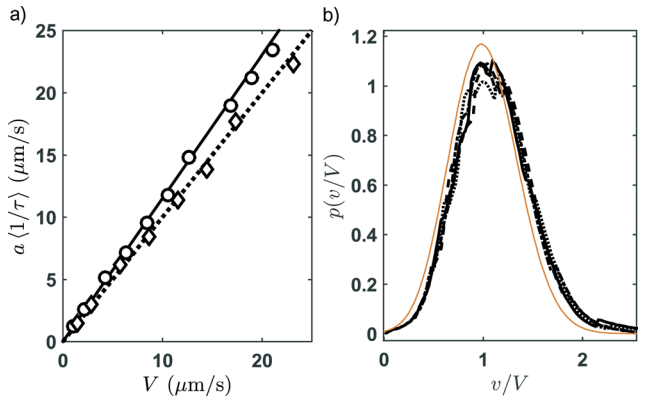

Fig. 7 (a) Mean velocity in the porous medium (circles) determined for various flow rates $Q = NSV$. The calibration factor a comes from the single channel experiment. The data are averaged over all the pore spaces of the micromodel. The solid line, of slope 1.15, corresponds to the best linear fit to the data. The slope of the dotted line is 1. The diamonds correspond to the averaged velocity in the injection channels. (b) Probability density functions of the normalized velocity in the porous medium. The thin solid line corresponds to the pore network simulations. It is well adjusted by a Gaussian function with a mean value of 1 and a standard deviation of 0.34. The other lines (dotted, dashed, solid and dash-dotted) are obtained from experiments carried out at various flow rates (1.1×10^{-10} m^3 s^{-1}, 1.4×10^{-10} m^3 s^{-1}, 2.2×10^{-10} m^3 s^{-1} and 2.8×10^{-10} m^3 s^{-1}, respectively).

pump to the network (see Fig. 7a), and we obtained a satisfying agreement between these measurements and the calibration curve obtained from the measurement in straight channels (see diamonds in Fig. 5). Several arguments might be proposed to explain the over-estimation of the fluid velocity. First, the velocity $V = Q/NS$ does not account for the contribution of the nodes of the network, while they represent about 20% of the total volume. Since one node connects two channels, the velocity in the nodes is higher and the mean velocity measured is then higher than V. Second, we cannot exclude that the poor resolution prevents correct measurements of the low flow velocity near the walls, which would also lead to an overestimation of the flow velocity.

To stress on the potential of our method, we made a close-up of the inlet sections and of a small part of the network, as shown in Fig. 6b. The inlet consists of straight channels divided into two equal channels in order to distribute the fluid equally over the full length of the chip. This part is thus made of branches with right angle corners: the method clearly highlights the low flow region appearing in this area. Likewise, in the area where the flow divides into two, the "jets" in the vertical walls can easily be distinguished. On the scale of a few pores, we see that the method makes the velocity contrast between the pores visible.

We also compared the velocity probability density functions (PDF). Due to the Newtonian nature of glycerol, once normalized by the average flow velocity $V = Q/NS$, the distribution should remain unaffected by any change in the average flow velocity. The results are shown in Fig. 7b. The collapse of the PDF obtained at various flow rates is excellent, which demonstrates the good quality of our measurement. The PDF are well described by Gaussian functions with standard deviations of around 0.35. The experimental results are compared to numerical simulation of the flow using a pore-network model approach. This method consists of assuming a developed laminar Poiseuille flow profile in each of the channels and solving the linear system of equations obtained by writing mass conservation in each node of the network (see Appendix for details). This allows one to calculate the PDF of the velocity for the network used experimentally. The PDF is displayed in Fig. 7b, together with the experimental data. As already discussed, the experimental mean value is slightly higher than the theoretical one, but one could see that the agreement on the standard deviation of the PDF is excellent.

We conclude that the auto-correlation technique combined with contrast reinforcement is well adapted to characterize flows in complex microfluidic networks.

Flow of a non-Newtonian liquid in a complex channel network

In order to illustrate the potential interest of our method, we used it to determine the flow structure of a complex fluid in the micromodel. Contrary to Netwonian fluid flows which could be easily predicted or modelled, characterizing the flow of non-Newtonian fluids in complex geometries is far more challenging because of the strong coupling between the geometry and the fluid properties. We choose to use a yield stress fluid, a carbopol gel. The main characteristic of this fluid is the existence of a yield stress σ_y (approx. 15 Pa). Consequently, the flow in a single channel only occurs when the pressure gradient at the pore scale $\Delta p/l$ overcomes the strain on its surface $2\sigma_y/W$. In a network of heterogeneous channels, one thus expects that for low flow rates, the flow is localized along a few paths, with the other channels being below the yield stress. The existence and characteristics of preferential paths have been predicted numerically[30,31] but not yet tested experimentally. One of the practical consequences of these preferential paths is to affect the global pressure drop/flow rate relation. The current scientific challenge is to determine the equivalent Darcy law for yield stress fluids. While most of the present studies focus on the macroscopic average flow velocity,[32] we see in Fig. 8 that our method makes it possible to study the details of the local flow structure.

The two velocity maps displayed in Fig. 8 are obtained with pressure ΔP close to the theoretical macroscopic yield stress pressure. As compared to the flow of a Newtonian fluid displayed in Fig. 6, the flow of the carbopol solution is much more heterogeneous. They both reveal the localization of the flow structure and the existence of preferential paths at a low flow rate. The flow heterogeneity due to the coupling between the network geometry and the non-linear flow properties of the carbopol solution is better evidenced by looking at the PDF of the velocity displayed in Fig. 8. They contrast with the ones obtained with the Newtonian fluid. The Gaussian distribution previously observed becomes an exponentially

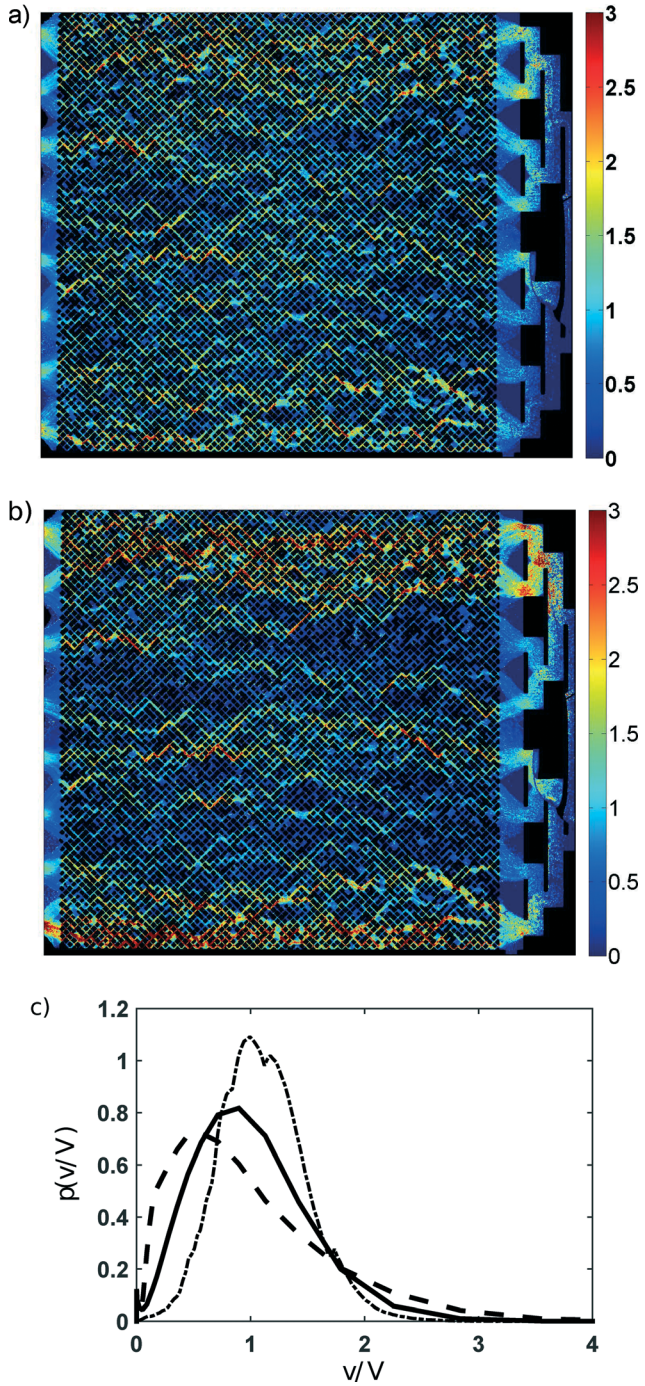

Fig. 8 (a and b) Velocity maps obtained with an aqueous carbopol solution. The two maps correspond to two different degrees of pressure applied: (a) ΔP = 7000 Pa (averaged velocity: V = 3.2 μm s^{-1}) and (b) 5000 Pa (V = 1.4 μm s^{-1}). (c) Distributions of the normalized velocity v/V in the two experiments shown above (solid and dashed lines) and of a Newtonian fluid (dotted line).

declining distribution, and the standard deviation increases when the flow rate is decreased. These distributions demonstrate that in some channels the flow is close to zero and is much larger than the average velocity in others. The quantitative analysis of such distributions is undoubtedly a relevant tool to study the evolution of the localization of the flow, but a quantitative and detailed study of this phenomenon is beyond the scope of the present article.

Discussion

In the previous sections, we have shown the validity and the potentiality of the auto-correlation method combined with contrast enhancement through a grid to map the velocity field in a complex microfluidic device. Let us now discuss in detail a few technical aspects which could benefit future users.

Let us first emphasize that the contrast enhancement through a grid is a powerful costless alternative to fluorescence optical methods. Although fluorescence microscopy is now a standard technique, it has some technical drawbacks and contraints. For instance, it requires suitable illumination devices and filters. The contrast enhancement by a grid only requires a grid and a standard camera and can achieve particle detection even when the tracer size is smaller than that of the pixel. Of course, the presence of the grid alters the quality of the raw image and induces some optical aberration as discussed in the experimental section. On the contrary, if the grid size becomes too small or if the spatial resolution is low in comparison with the mesh size, all the light deflected by the presence of the bead will be collected by the same pixel, thus cancelling the contrast enhancement effect. We therefore recommend to use a grid in which the wavelength is on the order of the pixel size. By doing so, the images are more uniform and do not suffer from the above-mentioned aberration. Standard sieves are good solutions to obtain grids of various wavelengths.

The auto-correlation method is very robust, as it could be used on poor quality images, contrary to PIV or PTV methods. The second advantage is related to the spatial resolution which is 1 pixel. Although the other methods could achieve this high resolution, they required averaging over a long period of time. In this paper, we use 3000 successive images to reach a precision of about 5%. The precision is reduced when using less images, but we obtain satisfactory results with only 500 images. As for other velocimetry methods, the frame rate needs to be adjusted to the magnitude of the velocity. Indeed, the characteristic time measured is inversely proportional to the velocity. In order for the auto-correlation function decay to be measured with good precision, the decorrelation $1/\tau_0$ time must be higher than the time between two successive images and lower than the maximal correlation time. We thus recommend to adapt the frame rate at about a few times $1/\tau_0$. Higher values would lead to better precision but would require a larger number of images. Although we restrict this study to low velocities (around 10 μm s^{-1}), the method could be applied without additional difficulties to larger velocities, provided that the acquisition frame rate f is set accordingly. The maximal velocity that could be measured is about af. The minimal velocity is about $af/(0.02N_0)$, where N_0 is the total number of images. The value of a is about the pixel size, as discussed below.

The tracer size should also be adapted to the experiments. Although large tracers lead to better optical contrast, they also reduce the spatial resolution and induce finite size bias when their size approaches a fraction of that of the channels. In this work, we used tracer sizes that are much smaller (6 μm or 20 μm beads) than the channel width and smaller or around the pixel size. The tracer concentration should also be adjusted since low concentrations require long acquisition time, and high concentrations influence the decorrelation time due to multiple particles. We thus recommend to adjust the concentrations so that the mean distance between tracers is approximately the channel height. Finally, the refractive index of the particles has a strong influence on the contrast and on the amplitude of the intensity fluctuations. Using water with a small amount of carbopol (n_1 = 1.33 (ref. 33)) instead of glycerol (n_1 = 1.47 (ref. 34)), we increased the difference between the refraction index of the tracer (n_2 = 1.49 for PMMA[35]) and of the fluid. We then observed an increase in the light intensity contrast that made it considerably easier to analyze the signals of the experiment displayed in Fig. 8 as opposed to the data displayed in Fig. 6.

The main drawback of the auto-correlation technique is that it requires a calibration procedure. The calibration factor a is a length scale which depends on the experimental parameters. Since the measured characteristic time corresponds to the passage of a tracer in front of a pixel, it should be – in principle – for tracers larger than the pixel size close to the tracer diameter or to the pixel size otherwise. For the data presented in this paper, we used 6 μm beads and a pixel size of about 20 μm. The characteristic size a found from velocity calibration is 10 μm. This is around both the bead and pixel sizes, which is thus coherent with the previous argument. We have tested several other experimental conditions. When the pixel size is much smaller than the beads, the value of a is clearly close to the bead diameter: we obtain a = 25.3 μm, with 20 μm beads and a pixel size of 0.17 μm. Increasing the pixel size leads to a more complex picture. With 6 μm beads, we have increased the pixel size, starting from 20 μm. We find that a increases from 10 to 18 μm when the pixel size is 40 μm but then saturates when the pixel size is increased further. Possibly the reason for saturation is related to the fact that for large pixel sizes, multiple beads could be observed at the same time on the same pixel. As the precise value of a depends on experimental conditions in addition to the details of the characteristic time definition (here, τ_0 has been defined as $C(\tau_0)$ = 0.5), we think the calibration step could not be avoided to achieve quantitative measurements. However, the value of the bead size could serve as an *a priori* estimation for the characteristic time.

Conclusion

In this work, we have shown that large scale anemometry with high resolution could be achieved efficiently and using time auto-correlation of the light intensity. The method is robust since it does not require high quality imaging of the tracer particles. In this work, we have used illumination through a grid to reinforce the contrast of the image and to achieve velocity mapping in bright field with beads smaller than the pixel size. Note that the time auto-correlation technique only estimates the velocity magnitudes and does not give information about the velocity direction. The combination of the two methods is thus of great interest to map velocity fields in a large complex microfluidic network. We have applied it to flows in micromodels of porous media, where high resolution velocimetry is required to achieve quantitative description of the phenomena. In addition to the experimental validation of the method using Newtonian fluids, we report preliminary results obtained with yield stress fluids which unambiguously show that the flow concentrates at low flow rates in preferential paths. The technique reported here thus opens the door to quantitative studies of complex fluid flows in model porous media.

Beyond the applications just mentioned, we are also convinced that this technique may be useful to study the flow structure of active fluids.[36–38] For instance, bacteria are characterized by a refractive index ($n_2 \approx 1.39$ (ref. 39 and 40)) slightly different from that of the suspending fluid (often a water solution with n_1 = 1.33) and have a typical size of a few microns. Our technique may then be useful to study the spatial organization of the velocity field of these fluids without the need to add tracer particles.

Appendix

The pore network modelling used to compute the theoretical PDF of the velocity inside the heterogeneous channel network consists of assuming developed flow profiles in all the rectangular channels. We use a similar network to that of the experiments, *i.e.* rectangular channels of uniform h but of heterogeneous width w_{ij}. These are set randomly according to a log-normal distribution having the same standard deviation as for the experiments. The channels are connected through nodes of the network where mass conservation written for a node labelled i simply reads

$$\sum_j Q_{ij} = 0, \tag{2}$$

where Q_{ij} is the flow rate in the channel connecting nodes i and j and where the summation is made on the neighboring nodes. The flow rate Q_{ij} is given for a Newtonian fluid by (ref. 41)

$$Q_{ij} = \frac{P_i - P_j}{\eta l}\frac{8h^4}{\pi^3}\sum_{n=1,3,5,\ldots}^{\infty}\frac{w_{ij}}{h\pi n^4} - \frac{2}{\pi^2 n^5}\tanh\left(\frac{n\pi w_{ij}}{2h}\right), \tag{3}$$

where η is the fluid viscosity, l is the length of the channel and P_i is the pressure at node i. This forms a complete set of linear equations of unknown P_i that we solve numerically using Matlab.

Knowing the pressure field, we then compute the mean velocities in all the channels to obtain the PDF displayed in Fig. 7.

Acknowledgements

The authors would like to thank J.-P. Hulin, D. Salin, L. Talon and T. Chevalier for useful discussions and the Agence Nationale de la Recherche for financial support of the project LaboCothep No. ANR-12-MONU-0011.

References

1 H. Stone, A. Stroock and A. Ajdari, *Annu. Rev. Fluid Mech.*, 2004, **36**, 381–411.
2 J. Santiago, S. Wereley, C. Meinhart, D. Beebe and R. Adrian, *Exp. Fluids*, 1998, **25**, 316–319.
3 D. Sinton, *Microfluid. Nanofluid.*, 2004, **1**, 2–21.
4 C. Cierpka and C. J. Kähler, *J. Visualization*, 2012, **15**, 1–31.
5 K. Hyoungsoo, J. Westerweel and G. E. Elsinga, *Meas. Sci. Technol.*, 2013, **24**, 024007.
6 Y. Zheng, J. Nguyen, Y. Weia and Y. Sun, *Lab Chip*, 2013, **13**, 2464–2483.
7 K. Drescher, J. Dunkel, L. H. Cisneros, S. Ganguly and R. E. Goldstein, *Proc. Natl. Acad. Sci. U. S. A.*, 2011, **108**, 10945.
8 D. Crandall, G. Ahmadi, D. Leonard, M. Ferer and D. H. Smith, *Rev. Sci. Instrum.*, 2008, **79**, 044501.
9 C. Perrin, P. Tardy, K. Sorbie and J. Crawshaw, *J. Colloid Interface Sci.*, 2006, **295**, 542–550.
10 C. Cottin, H. Bodiguel and A. Colin, *Phys. Rev. E: Stat., Nonlinear, Soft Matter Phys.*, 2010, **82**, 046315.
11 A. Clarke, A. M. Howe, J. Mitchell, J. Staniland, L. Hawkes and K. Leeper, *Soft Matter*, 2015, **11**, 3536–3541.
12 C. A. Conn, K. Ma, G. J. Hirasaki and S. L. Biswal, *Lab Chip*, 2014, **14**, 3968.
13 K. Ma, R. Liontas, C. A. Conn, G. J. Hirasaki and S. Biswal, *Soft Matter*, 2012, **8**, 10669.
14 H. Lee, S. G. Lee and P. S. Doyle, *Lab Chip*, 2015, **15**, 3047–3055.
15 M. Romano, M. Chabert, A. Cuenca and H. Bodiguel, *Phys. Rev. E: Stat., Nonlinear, Soft Matter Phys.*, 2011, **84**, 065302.
16 W. Song and A. R. Kovscek, *Lab Chip*, 2015, **15**, 3314–3325.
17 J. Beaumont, H. Bodiguel and A. Colin, *Soft Matter*, 2013, **9**, 10174–10185.
18 N. K. Karadimitriou, P. Nuske, P. J. Kleingeld, S. M. Hassanizadeh and R. Helmig, *Lab Chip*, 2014, **14**, 2515–2524.
19 M. Wu, F. Xiao, R. M. Johnson-Paben, S. T. Retterer, X. Yin and K. B. Neeves, *Lab Chip*, 2012, **12**, 253–261.
20 N. S. K. Gunda, B. Bera, N. K. Karadimitriou, S. K. Mitra and S. M. Hassanizadeh, *Lab Chip*, 2011, **11**, 3785–3792.
21 J. Gauteplass, K. Chaudhary, A. R. Kovscek and M. A. Fernø, *Colloids Surf., A*, 2015, **468**, 184.
22 J. Westerweel, P. F. Geelhoed and R. Lindken, *Exp. Fluids*, 2004, **37**, 375.
23 H.-S. Chuang, L. Gui and S. T. Wereley, *Microfluid. Nanofluid.*, 2012, **13**, 49–64.
24 S. T. Wereley and C. D. Meinhart, *Annu. Rev. Fluid Mech.*, 2010, **42**, 557–576.
25 C. J. Kaehler, S. Scharnowski and C. Cierpka, *Exp. Fluids*, 2012, **52**, 1629–1639.
26 B. R. Sutherland, S. B. Dalziel, G. O. Hughes and P. F. Linden, *J. Fluid Mech.*, 1999, **390**, 93–126.
27 S. B. Dalziel, O. H. Graham and B. R. Sutherland, *Exp. Fluids*, 2000, **28**, 322–335.
28 C. B. B. Geraud and L. Bocquet, *Eur. Phys. J. E: Soft Matter Biol. Phys.*, 2013, **36**, 30.
29 F. M. White, *Fluid Mechanics*, McGraw-Hill, New York, 2003.
30 L. Talon and D. Bauer, *Eur. Phys. J. E: Soft Matter Biol. Phys.*, 2013, **36**, 139.
31 T. Chevalier and L. Talon, *Phys. Rev. E: Stat., Nonlinear, Soft Matter Phys.*, 2015, **91**, 023011.
32 T. Chevalier, C. Chevalier, X. Clain, J. Dupla, J. Canou, S. Rodts and P. Coussot, *J. Non-Newtonian Fluid Mech.*, 2013, **195**, 57–66.
33 A. Harvey, J. S. Gallagher and J. M. H. L. Sengers, *J. Phys. Chem. Ref. Data*, 1998, **27**, 761.
34 L. F. Hoyt, *Ind. Eng. Chem.*, 1934, **26**, 329–332.
35 P. Michela, J. Dugasa, J. M. Carioua and L. Martina, *J. Macromol. Sci., Part B: Phys.*, 1985, 379–394.
36 J. Gachelin, A. Rousselet, A. Lindner and E. Clément, *New J. Phys.*, 2014, **16**, 02.
37 H. M. Lopez, J. Gachelin, C. Douarche, H. Auradou and E. Clément, *Phys. Rev. Lett.*, 2015, **115**, 028301.
38 A. Creppy, O. Praud, X. Druart, P. Kohnke and F. Plouraboué, *Phys. Rev. E: Stat., Nonlinear, Soft Matter Phys.*, 2015, **92**, 032722.
39 A. E. Balaev, K. N. Dvoretski and V. A. Doubrovski, *Proc. SPIE 5068, Saratov Fall Meeting 2002: Optical Technologies in Biophysics and Medicine IV*, 375 (October 14, 2003), DOI: 10.1117/12.518853.
40 P. Y. Liu, L. K. Chin, W. Ser, T. C. Ayi, P. H. Yap, T. Bourouina and Y. Leprince-Wang, *Procedia Eng.*, 2014, **87**, 356–359.
41 N. Mortensen, F. Okkels and H. Bruus, *Phys. Rev. E: Stat., Nonlinear, Soft Matter Phys.*, 2005, **71**, 057301.